


SCIENTIFIC REPORTS

OPEN

δ -MnO₂ nanoflower/graphite cathode for rechargeable aqueous zinc ion batteries

Sonti Khamsanga¹, Rojana Pornprasertsuk^{2,3,4}, Tetsu Yonezawa⁵, Ahmad Azmin Mohamad⁶ & Soorathep Kheawhom^{1,3} 

Manganese oxide (MnO₂) is one of the most promising intercalation cathode materials for zinc ion batteries (ZIBs). Specifically, a layered type delta manganese dioxide (δ -MnO₂) allows reversible insertion/extraction of Zn²⁺ ions and exhibits high storage capacity of Zn²⁺ ions. However, a poor conductivity of δ -MnO₂, as well as other crystallographic forms, limits its potential applications. This study focuses on δ -MnO₂ with nanoflower structure supported on graphite flake, namely MNG, for use as an intercalation host material of rechargeable aqueous ZIBs. Pristine δ -MnO₂ nanoflowers and MNG were synthesized and examined using X-ray diffraction, electron spectroscopy, and electrochemical techniques. Also, performances of the batteries with the pristine δ -MnO₂ nanoflowers and MNG cathodes were studied in CR2032 coin cells. MNG exhibits a fast insertion/extraction of Zn²⁺ ions with diffusion scheme and pseudocapacitive behavior. The battery using MNG cathode exhibited a high initial discharge capacity of 235 mAh/g at 200 mA/g specific current density compared to 130 mAh/g which is displayed by the pristine δ -MnO₂ cathode at the same specific current density. MNG demonstrated superior electrical conductivity compared to the pristine δ -MnO₂. The results obtained pave the way for improving the electrical conductivity of MnO₂ by using graphite flake support. The graphite flake support significantly improved performances of ZIBs and made them attractive for use in a wide variety of energy applications.

Manganese dioxide (MnO₂) is widely used as a cathode material in battery technologies because of its several advantageous properties such as low-cost, abundant, low toxicity, and environmental friendliness^{1–3}. MnO₂ were previously studied and applied for a variety of energy storage devices^{4–7}. Also, it was applied in different metal-ion batteries including Li-ion battery (LIB)⁸, Mg-ion battery (MIB)⁹ and Zn-ion battery (ZIB)^{10,11}. MnO₂ cathodes are inexpensive and exhibit a high theoretical capacity. Recently, aqueous Zn/MnO₂ batteries are considered as promising alternative energy devices due to their high safety and the abundance of both Zn, MnO₂ and the electrolyte^{12–14}.

However, MnO₂ suffers from its poor conductivity that often occurs in high internal resistance of the electrode resulting in poor performance of the battery¹⁵. Therefore, to improve the performance of the MnO₂ cathode, it is necessary to increase the specific surface area of MnO₂ as well as the ion diffusion rate^{16,17}. MnO₂ has various crystallographic polymorphs such as α -MnO₂, β -MnO₂, and δ -MnO₂, etc. Among these, δ -MnO₂ was reported to be a potential intercalation host material for aqueous ZIBs¹⁸ due to a substantial interlayer distance for the reversible insertion/extraction of Zn²⁺ ions. δ -MnO₂ can be prepared by a chemical reduction or hydrothermal process¹⁹. The conventional synthesis method is the direct reduction of KMnO₄ aqueous solution by dropwise introduction of concentrated HCl. Previously, δ -MnO₂ nano-flakes were synthesized and used in aqueous ZIBs¹⁸. It led to a significant increase in the power density of the ZIB. Another approach undertaken was to support MnO₂ nanostructures on a matrix material with a high surface area^{5,20,21}. It was observed that these nanostructures could accelerate

¹Department of Chemical Engineering, Faculty of Engineering, Chulalongkorn University, Bangkok, 10330, Thailand.

²Department of Materials Science, Faculty of Science, Chulalongkorn University, Bangkok, 10330, Thailand.

³Research Unit of Advanced Materials for Energy Storage, Chulalongkorn University, Bangkok, 10330, Thailand.

⁴Center of Excellence in Petrochemical and Materials Technology, Chulalongkorn University, Bangkok, 10330, Thailand.

⁵Division of Materials Science and Engineering, Faculty of Engineering, Hokkaido University, Kita 13 Nishi 8, Sapporo, Hokkaido, 060-8628, Japan.

⁶School of Materials and Mineral Resources Engineering, Universiti of Sains Malaysia, 14300 Nibong Tebal, Pulau Pinang, Malaysia. Correspondence and requests for materials should be addressed to S. Kheawhom (email: soorathep.k@chula.ac.th)

the charge transport during the electrochemical redox process. In this respect, various carbonaceous materials, namely activated carbon, carbon nanotubes (CNTs), carbon nanofibers (CNFs), graphene and graphite, have been integrated with MnO₂. MnO₂/graphene nanoflowers were synthesized in the form of sandwich-structured nanoflowers which exhibited excellent super capacitive properties effectively making a very conductive electrode material for high-performance super capacitors²². However, it is significant that MnO₂ supported on graphite has not been reported previously in ZIBs application. The crystal structure of graphite consists of parallel planes of carbon atoms which is conductive primarily along its planes^{23,24}. In this way, graphite is classified as a semimetal due to its high electrical conductivity²⁵. Therefore, MnO₂ supported on graphite is considered as the candidate due to an improvement in electronic conductivity and an increase in the stability of the electrode materials for ZIBs.

The present study reports on δ -MnO₂ nanoflower/graphite as a cathode host material for rechargeable aqueous ZIBs. The δ -MnO₂ nanoflower supported on graphite not only increases the electrical conductivity and discharge capacity of the battery but also improves the insertion/extraction acceleration by increasing the active area of the δ -MnO₂ nanoflower. Accordingly, the electrochemical properties and performances of the batteries which use the MNG as host material cathode are examined and discussed.

Experimental

Chemical and materials. Reagent grade chemicals were obtained and used without further purification unless noted otherwise. The graphite powder was purchased from Aldrich Company. Potassium permanganate (KMnO₄), manganese sulfate monohydrate (MnSO₄·H₂O), zinc sulfate (ZnSO₄), sulfuric acid (H₂SO₄), and cellulose acetate were purchased from Ajax Finechem. Nickel foam (0.5 mm thick, 100 PPI) was purchased from Qijing Trading Co., Ltd. Whatman filter paper No.1 was purchased from Sigma-Aldrich. Graphite foil was purchased from Shenzhen 3KS Electronic Material Co. Ltd. Zn sheet (99.99%) was purchased from Sirikul Engineering Ltd., Part.

Preparation of δ -MnO₂ nanoflower and δ -MnO₂ nanoflower/graphite (MNG). The pristine δ -MnO₂ nanoparticles were synthesized by dissolving KMnO₄ (1.98 g) in 60 mL of deionized (DI) water. Then, MnSO₄·H₂O (0.336 g) was dissolved in 20 mL of DI water. Next, the MnSO₄·H₂O solution was added dropwise to the KMnO₄ solution, and continuous stirring followed for 30 min. Afterward, the mixture was transferred into a 100 mL Teflon autoclave and kept at 160 °C for 24 hr in an oil bath. The product was collected and washed with DI water several times. Then, it was dried at 80 °C for 12 hr. The MNG synthesis was similar to the method reported by Liu *et al.*²² with some modifications. Graphite (1.0 g) was mixed in DI water (500 mL) with KMnO₄ (10.0 g). The mixture of graphite and KMnO₄ was stirred for 18 hr. Then, 98% of H₂SO₄ (5 mL) was added dropwise into the mixture. The solution was continuously stirred for 1 hr and heated to and maintained at 80 °C for 1 hr. After that, the solution was diluted in 1 L of DI water and allowed to stand at room temperature. The solution was filtered using cellulose filter paper (pore size 11 μ m). Then, the MNG precipitates were collected and washed by DI water several times until the violet color disappeared. Subsequently, the precipitates were dried at 80 °C overnight.

Characterization and electrochemical measurement. X-ray Diffraction (XRD, Bruker AXS Model D8 Discover) of the powder samples was carried out with Cu K α radiation at a scanning range of 5–80°. Field Emission Scanning Electron Microscope (FESEM, JEOL JSM-7610F, Tokyo, Japan) was used to take the morphology image and nanoflower size of MNG.

The cathode using MNG was prepared by mixing together 70% wt. of MNG, 20% wt. of carbon black (CB), and 10% wt. of cellulose acetate binder. Alternatively, the cathode using pristine δ -MnO₂ was prepared by mixing together 70% wt. of the pristine δ -MnO₂, 20% wt. of carbon black (CB), and 10% wt. of cellulose acetate binder. Acetone was used to adjust the viscosity of the slurries. Each mixed slurry was coated on graphite foil using a lab coating machine (AOT-FCM-250, AOT Electronic Technology Co., LTD) and dried at 70 °C under vacuum. The thickness of the cathode material deposited was 25 μ m. The zinc anode was prepared by electrodeposition of zinc from ZnSO₄ (0.5 M) aqueous solution onto Ni-foam using zinc sheet as a counter electrode at the current density of 60 mA/cm². The amount of zinc deposited was 20 mg/cm². Both cathode and anode were punched into a 15 mm diameter disk. The filter paper was punched into a 19 mm disk and used as the separator. Then, 0.3 mL of ZnSO₄ (1 M) was added to the cell. The testing cells were fabricated as a coin cell (CR2032).

Electrochemical measurements were carried out using a CR2032 coin cell. Cyclic Voltammetry (CV) was performed by Potentiostat (VersaStat3, Princeton Applied Research) at a scan rate of 0.5 mV/s in the voltage range 1.0–1.8 V versus Zn²⁺/Zn. A battery testing system (BTS-5V10mA, Neware, China) was used to investigate the performance of the battery. The charge-transfer resistance, as illustrated by the Nyquist plots for the cathode, was carried out using an Electrochemical Impedance Spectroscopy (EIS) technique using an amplitude of 10 mV in the frequency range of 1–100,000 Hz.

Results and discussion

In this study, δ -MnO₂ nanoflower/graphite (MNG) was prepared by a modified method of Liu *et al.*²². In Fig. 1, the XRD patterns of δ -MnO₂ and graphite are shown. Thus, it can be seen that both patterns, i.e. δ -MnO₂ (JSPDS card no. 80–1098)^{26,27} and graphite (JSPDS card no. 41–1487)²⁸ match well. In the XRD pattern of MNG. The diffraction peaks (2 θ) at 12.2°, 26.5°, 36.6°, and 65.6° correspond to the (001), (002), (–111) and (–312) crystal planes of δ -MnO₂, respectively²⁹. The high-intensity diffraction peak of MNG at 26.5° indicates the high crystallinity of graphite. δ -MnO₂ possesses a planar layered-structure as illustrated by the inset of Fig. 1. This structure suggests that the interlayer gap is easy to insert/extract foreign cations and thereby can be useful for energy

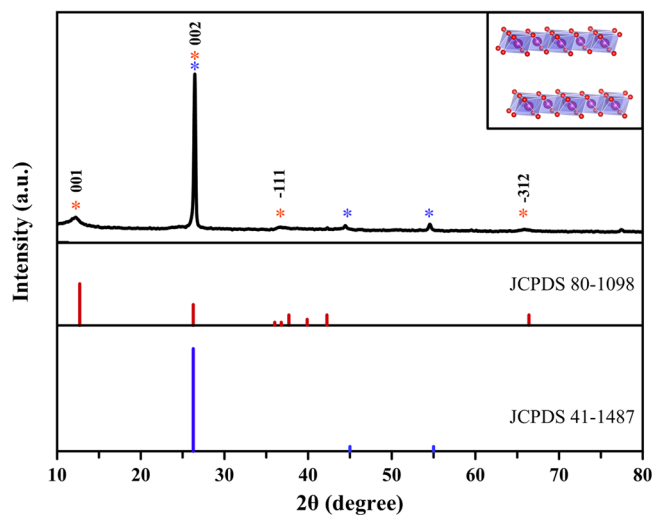


Figure 1. XRD pattern of the synthesized δ -MnO₂ nanoflower/graphite (MNG) and crystallographic structure of δ -MnO₂ (inset).

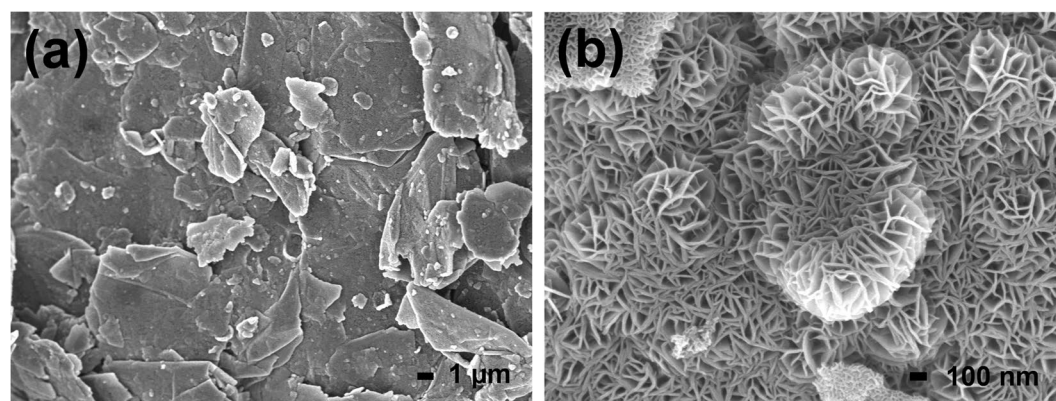
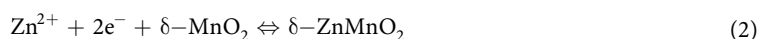


Figure 2. FESEM images of the synthesized δ -MnO₂ nanoflower/graphite (MNG): (a) low magnification image, and (b) high-magnification image.

storage applications²⁷. Further, the XRD analysis confirmed that the delta (δ) phase was presented in the pristine δ -MnO₂ sample (see Supplementary Information Fig. S1).

In Fig. 2(a), the FESEM image of MNG is shown. It is observed that the numerous MnO₂ nanoflowers constructed on the graphite surface reveal a flake-like sample. Figure 2(b) shows the higher magnification image of MNG which indicates that many petals can interconnect forming micropores about 50 nm in diameter size. The MNG having micropores among petals will assist in increasing the contact area between the electrolyte and cathode material as well as ensure fast ion transfer in the charge/discharge process²².

In Fig. 3, the battery configuration in this study which is composed of the MNG cathode, zinc anode, and ZnSO₄ aqueous electrolyte is shown. During discharging, anodic zinc is dissolved in the form of Zn²⁺ ions into an aqueous electrolyte, containing Zn²⁺ ions and rapidly solvate in the form of solvated Zn²⁺ ion. Then, they diffuse and pass through the separator to the MNG cathode. The solvated Zn²⁺ ions are de-solvated in the form of Zn²⁺ ions and intercalate into δ -MnO₂ structure^{30,31} as illustrated by the inset of Fig. 3. Further, an electron current starts to flow in the electrical loop from the electrical conduction of graphite. These three processes can be reversed by (1) the de-intercalation of Zn²⁺ ions from MNG cathode; then (2) solvated species are formed and lastly (3) Zn²⁺ ions are reduced to Zn and deposited back on the zinc anode, respectively. The electrochemical reaction may be expressed as in Eq. (1) anode reaction and Eq. (2) cathode reaction:



During the electrochemical Zn²⁺ ion insertion¹³, the layered type δ -MnO₂ structure can transform to spinel-type ZnMn₂O₄ with Mn(III) state and layered type δ -Zn_xMnO₂ with Mn(II) state.

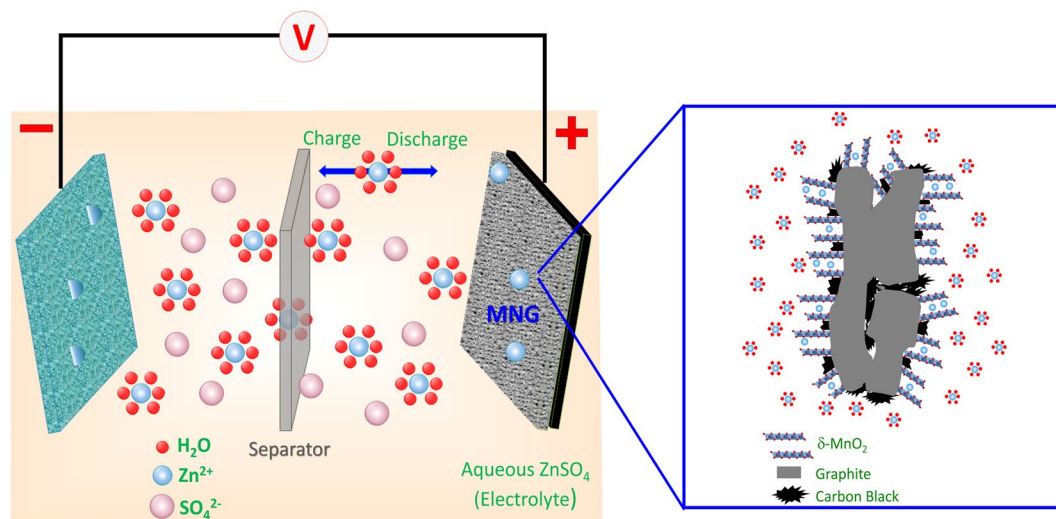


Figure 3. Schematics of the chemistry of the zinc-ion battery. Zn^{2+} ions migrate between tunnels of the MNG cathode and Zn anode. The inset on the right shows Zn^{2+} ion insertion and interconnection between $\delta\text{-MnO}_2$ and graphite.

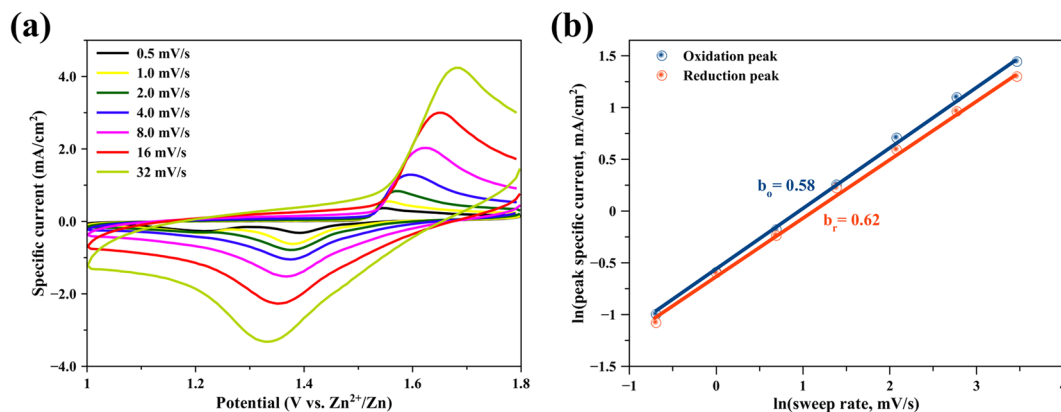


Figure 4. (a) Cyclic voltammograms of $\delta\text{-MnO}_2$ nanoflower/graphite (MNG) cycling at different sweep rates, and (b) the fitted lines: $\ln(\text{peak specific current})$ versus $\ln(\text{sweep rate})$.

To investigate the kinetics of the MNG electrode, cyclic voltammograms using sweep rates of 0.5 to 32 mV/s in the voltage range 1.0–1.8 V versus Zn^{2+}/Zn were measured using CR2032 coin cells. As shown in Fig. 4(a), a dominating pair of redox peaks exhibits increasing currents when the sweep rates increase, which do not display rectangular-shape and symmetrical voltammograms even at high scan rates, compared to MnO_2 /activated carbon composite for supercapacitors³². It is noted that the MNG electrode does not present the capacitive behavior of the electrode^{33,34}. The capacitive effect is characterized by analyzing the cyclic voltammetry data at different sweep rates as in Eq. (3):

$$i = av^b \quad (3)$$

where i is the peak specific current, v is a potential sweep rate and a , b are adjustable parameters. The redox reaction is limited by the diffusion-controlled behavior; the peak current i varies as $v^{1/2}$. Although the capacitance contribution suggests that the peak current i varies as $v^{35,36}$. Equation (3) can be taken with logarithm and can be expressed according to Eq. (4):

$$\ln i = b \ln v + \ln a \quad (4)$$

The b value denotes the slope of the plot of $\ln i$ versus $\ln v$. When b value is close to 1, the system is mainly controlled by capacitance; when b value is close to 0.5, the Zn^{2+} ion insertion process dominates. Figure 4(b) shows the $\ln i$ versus $\ln v$ plots at oxidation and reduction process of the cyclic voltammogram. The b_o (oxidation process) and b_r (reduction process) of the MNG cathode are 0.58 and 0.62, respectively. Since the average b values are close to 0.5, it may imply that the redox reactions on the MNG cathode are controlled by the diffusion process. MnO_2

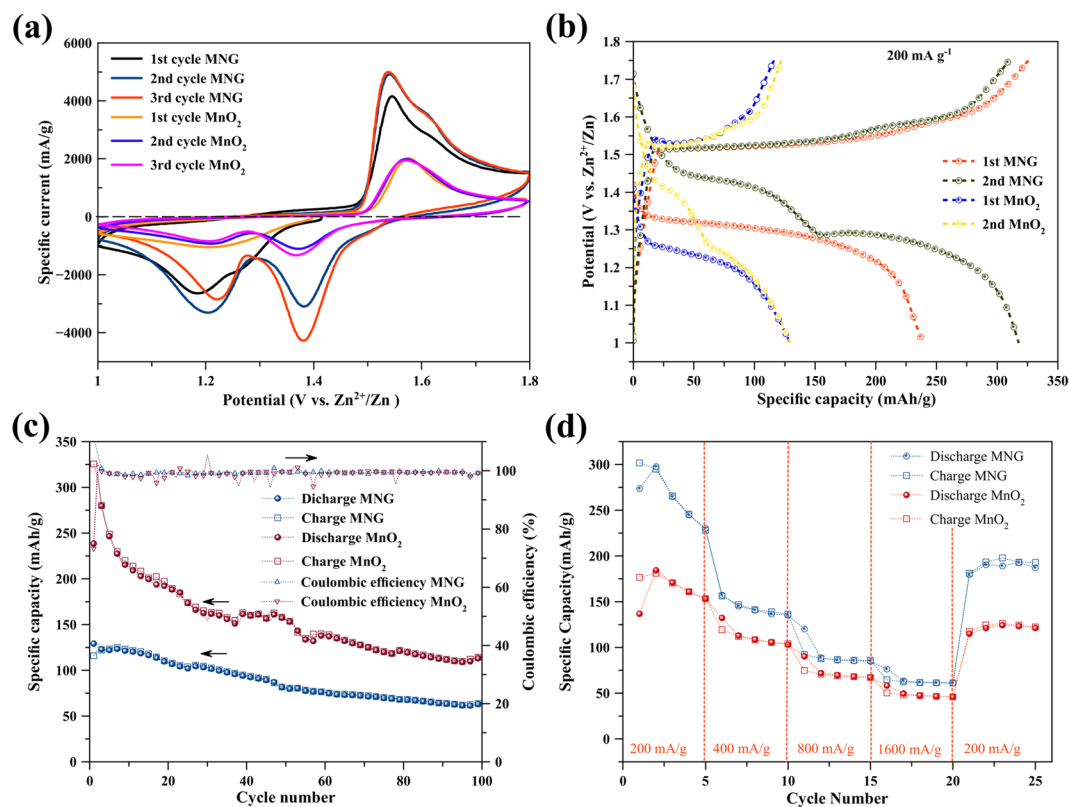


Figure 5. Performances of the batteries: (a) cyclic voltammograms of the batteries at a scan rate of 0.5 mV/s, (b) galvanostatic charge-discharge profile of the batteries at 200 mA/g, (c) cycling performance of the batteries at 400 mA/g, and (d) rate capability of the batteries at different discharge rates.

is a transition metal oxide that typically displays the pseudocapacitance behavior³⁷. The capacitive-controlled process occurs only on the surface. However, in the case of MNG cathode, the characteristic of Zn^{2+} ions insertion/extraction deviates from capacitive-controlled process towards the diffusion-controlled process. That is, the insertion/extraction of Zn^{2+} ions occur not only on the surface but also the pores inside. The result shows good agreement of a fast Zn^{2+} ion insertion/extraction or high rate property for the battery³⁵.

In order to compare the improved electrochemical properties of MNG as the cathode for ZIB, the pristine $\delta\text{-MnO}_2$ is used as a comparable cathode. Figure 5 (a) shows the CV profiles of the pristine $\delta\text{-MnO}_2$ and MNG electrodes at a scan rate of 0.5 mV/s over the potential range 1.0–1.8 V for the initial three cycles. During the first cycle, two distinct peaks are observed at 1.20 and 1.57 V for the pristine $\delta\text{-MnO}_2$ electrode and at 1.18 and 1.54 V for MNG. The peaks in the low potential region appear at 1.20 and 1.18 V which can be attributed to Zn^{2+} ion insertion into the $\delta\text{-MnO}_2$ host structure. In the higher potential region, two oxidation peaks can be seen at 1.57 and 1.54 V for $\delta\text{-MnO}_2$ and MNG, respectively, which correspond to the extraction of Zn^{2+} ions from the $\delta\text{-MnO}_2$ host structure. The results suggest that, the oxidation state of Mn is reduced to Mn^{3+} states and is oxidized back to Mn^{4+} states, during Zn^{2+} ion insertion and extraction, respectively^{13,14,18,38}. On subsequent cycling, two distinct peaks appear at 1.37 and 1.21 V for Zn^{2+} ion insertion into $\delta\text{-MnO}_2$ whereas the peaks at 1.38 and 1.20 V were observed for MNG in the low voltage region. In the high voltage region, the peak at 1.57 and shoulder at 1.62 V can be clearly seen for the pristine $\delta\text{-MnO}_2$. Likewise, the peak at 1.53 V and shoulder at 1.60 V can be clearly seen for the MNG electrodes. The cyclic voltammogram, having two peaks during discharge and having a peak with shoulder during charge, exhibits typical characteristics of the electrochemical insertion/extraction of Zn^{2+} ions in MnO_2 structure^{12,13,39–41}. These results with two peaks during discharge may be more clearly described by the two-step reaction of Zn^{2+} ion insertion in electrochemical reaction^{12,38} and spinel-type ZnMn_2O_4 transformation³³. In the following scan cycles, the peaks at 1.37 V for $\delta\text{-MnO}_2$ and at 1.38 for MNG increase gradually during discharge indicating an activation process³⁸. The CV curve of MNG exhibits a higher peak intensity and a larger enclosed area when compared with the pristine $\delta\text{-MnO}_2$ indicating improved electrochemical performance and fast Zn^{2+} ion insertion/extraction⁴².

Figure 5(b) shows the first and second discharge/charge profiles of the pristine $\delta\text{-MnO}_2$ and MNG cathode in a coin cell battery when cycled at a specific current density of 200 mA/g in the potential range of 1.0–1.8 V. The battery fabricated with the pristine $\delta\text{-MnO}_2$ and MNG host cathode material under open air condition displays an open-circuit voltage (OCV) of about 1.4 V. The first discharge capacity for MNG is 235 mAh/g whereas the pristine $\delta\text{-MnO}_2$ registers only 130 mAh/g. Compared to todorokite-type MnO_2 ¹⁴ and $\delta\text{-MnO}_2$ nano-flake¹³, the initial discharge capacity can deliver only 98 mAh/g (at 50 mA/g) and 122 mAh/g (at 83 mA/g), respectively. It is clear that $\delta\text{-MnO}_2$ supported on graphite samples can accommodate more numbers of Zn^{2+} ions than the

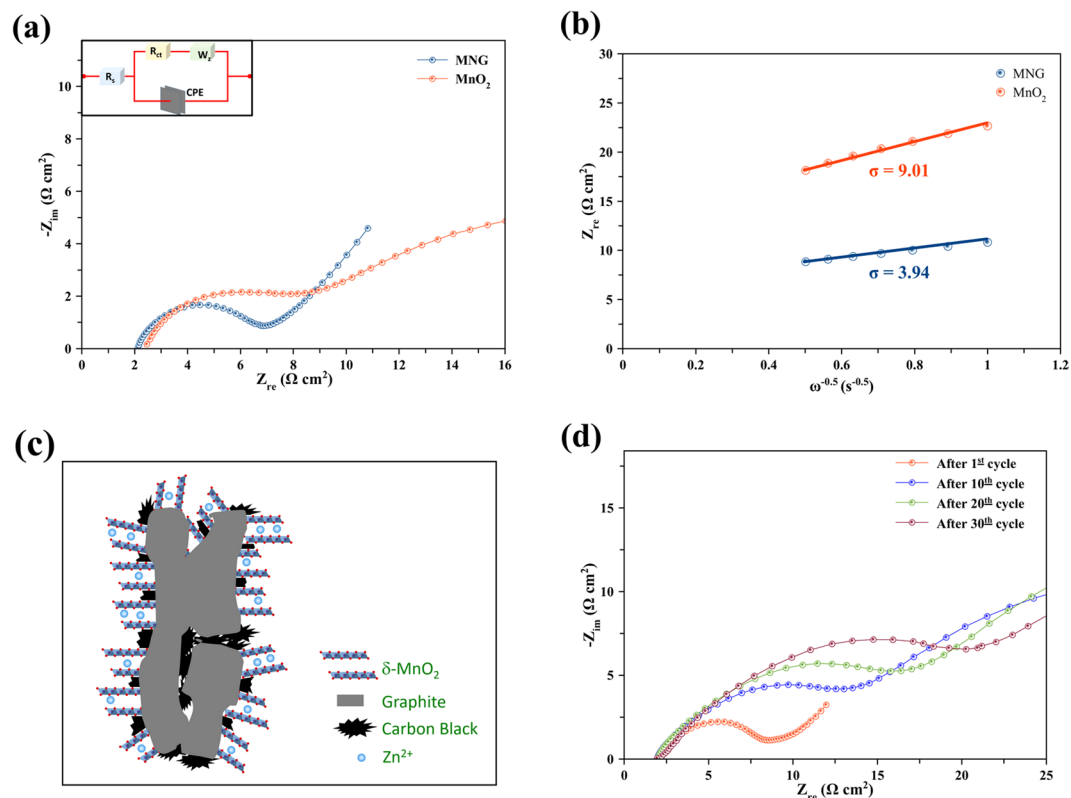


Figure 6. EIS results of the batteries: (a) Nyquist plot of EIS spectra, (b) relationship between real part of impedance versus $\omega^{-0.5}$ for the batteries using MNG and the pristine δ -MnO₂, (c) schematic illustration for the Zn²⁺ ion insertion into the MNG electrode, and (d) Nyquist plot of EIS spectra of MNG at various charge/discharge cycles.

unsupported δ -MnO₂ (pristine δ -MnO₂). It appears that the nanoflower δ -MnO₂ in the structure of MNG tend to enhance the electrode/electrolyte contact area, thereby favoring Zn²⁺ ion insertion⁴¹. In addition, MNG shows a longer horizontal discharge curve than that of δ -MnO₂, suggesting a more stable Zn²⁺ ion insertion into the MNG than in the pristine δ -MnO₂. On the subsequent cycle, during the continuous discharge, the voltage profiles present two distinct plateaus at 1.45 and 1.25 V for MNG and 1.4 and 1.2 V for δ -MnO₂. These characteristics were also observed for MnO₂ electrodes in aqueous ZIB systems^{14,43}. It can be implied that Zn²⁺ ions can insert into the layered δ -MnO₂³⁹ which is in agreement with the two distinct peaks during discharge, as shown in Fig. 5(a).

Figure 5(c) displays the cycling behavior and corresponding coulombic efficiency of the pristine δ -MnO₂ and MNG electrodes, under the specific current density of 400 mA/g. At the 100th cycle, the discharge and charge capacities registered by δ -MnO₂ were 63.3 and 63.8 mAh/g, respectively while that of MNG were 113.4 and 114.2 mAh/g, respectively. The lower capacity retention of δ -MnO₂ may result from low intrinsic electronic conductivity because of the appearance of unstable Mn³⁺ states during zinc-ion insertion¹⁰. The higher capacity retention of MNG may indicate that the electronic conductivity of MNG is improved. In the initial cycles, gradual capacity fade was observed for the pristine δ -MnO₂ electrode, but fast capacity fade was observed for the MNG electrode. The formation of ZnMn₂O₄ with the Jahn-Teller Mn³⁺ ion may contribute to electrode degradation and hence lead to the fast capacity fade¹³. However, MNG demonstrates higher capacity than the pristine δ -MnO₂. Over long-term cycling, the coulombic efficiency of both host material electrodes is maintained at around 100%. Thus, this clearly demonstrates that no irreversible capacity losses occurred⁴¹.

In Fig. 5(d), the rate performances of the pristine δ -MnO₂ and MNG host material cathodes are shown. Cycling takes place at various specific current densities of 200, 400, 800 and 1600 mA/g, namely 5 times for each rate. The rate performance of MNG is significantly higher than those of the pristine δ -MnO₂. It is indicated that nanoscale morphology of δ -MnO₂ nanoflowers on graphite increases the contact area between the electrode and the electrolyte and provides more electrochemically active sites for ion-insertion¹³. Graphite not only improves the electronic conductivity of the MNG electrode but also tends to disperse the δ -MnO₂ nanoflower sites. The MNG cathode can be charged and discharged at different rates; a high rate of 1600 mA/g leads to a discharge and charge capacity of 76 and 64 mAh/g, respectively. When cycled at a specific current density of 200 mA/g, the MNG cathode can deliver a discharge and charge capacity of 181 and 179 mAh/g, respectively. This behavior indicates that the MNG cathode can well be considered for the Zn²⁺ ion storage material¹⁰. It is clear therefore that MNG can improve not only the cycling performance but also the rate performance for ZIBs.

As displayed in Fig. 6(a), the difference in electrochemical conductivity before cycling between the pristine δ -MnO₂ and MNG host cathodes was examined using EIS. The curves of the pristine δ -MnO₂ and MNG host cathodes consist of depressed semicircles and diffusion drift which can be perfectly fitted using Randles

equivalent circuit (see Inset Fig. 6(a)). Hence, in the equivalent circuit, R_s is the solution resistance, R_{ct} is the charge-transfer resistance at the interfaces and Z_w is the Warburg impedance related to the diffusion of Zn^{2+} ions. The R_{ct} value for the pristine δ - MnO_2 is 5.9 Ω and the value reduces to 4.8 Ω when supported on graphite (MNG). The result indicates that the electrical conductivity of the MNG sample is improved by constructing a conductive support using the graphite. The relationship between real impedance (Z') and angular frequency (ω) in the low frequency region can be expressed accordingly by Eq. (5)⁴⁴:

$$Z' = R_s + R_{ct} + \sigma\omega^{-0.5} \quad (5)$$

where σ is the Warburg factor which is relative to $Z' - \omega$ obtained from the slope of the lines in Fig. 6(b). The diffusion coefficient of zinc ion can be calculated as in Eq. (6)⁴⁵:

$$D = R^2 T^2 / 2 A^2 n^4 F^4 C^2 \sigma^2 \quad (6)$$

where R is the gas constant, T is the absolute temperature, n is the number of electrons per molecule oxidized, A is the surface area, F is Faraday's constant, C is the concentration and D is the diffusion coefficient.

As shown in Fig. 6(b), the slope which is the σ value of MNG (3.94) host electrode is lower than that of the pristine δ - MnO_2 (9.01) indicating that the diffusion coefficient of MNG is higher than that of the pristine δ - MnO_2 , as in Eq. (6). It is clear that the MNG host material electrode can enhance the diffusion coefficient of Zn^{2+} ion, highlighting the electrical conductivity improvement^{44,46}.

In Fig. 6(c), the MNG cathode which is a δ - MnO_2 structure supported on graphite is drawn and illustrated. It is highly possible that Zn^{2+} ions can insert into the δ - MnO_2 nanoflower structure having short diffusion length. Thereby, electrochemical performance can be improved during cycling at high rate⁴⁷.

In Fig. 6(d), after charge/discharge cycling, the EIS measurements of MNG are shown. After the 1st, 10th, 20th, and 30th cycles, the MNG host cathode exhibits the R_{ct} values, namely 6.51, 10.9, 13.7 and 18.2 Ω , respectively. After the first cycle, the charge-transfer resistance increases which indicates that the intercalation of Zn^{2+} ions into the δ - MnO_2 structure becomes more difficult. The conduction of ions before intercalation depends not only on the cathode material but also on the electrolyte access into the cathode. The porosity of the cathode material is an important factor which can affect the electrolyte access. The SEM image of MNG and the pristine δ - MnO_2 compound is displayed in the Supplementary Information Fig. S2.

Conclusion

In summary, δ - MnO_2 nanoflower supported on graphite flake was synthesized and used as an intercalation host material for a rechargeable ZIB. While the XRD studies confirmed the crystallographic structure, the FESEM studies revealed that the sample showed a nanoflower-like morphology having micropores about 50 nm in diameter. This study demonstrates that a diffusion process controlled the electrochemical reactions of the MNG cathode. When tested in ZIB, the MNG sample registered a prominent discharge capacity of 235 mAh/g, which was higher than the discharge capacity of pristine δ - MnO_2 (130 mAh/g). After the 100th cycle, the discharge capacity registered by the δ - MnO_2 was only 63.3 mAh/g whereas the MNG delivered a discharge capacity of 113.4 mAh/g. Moreover, the conductivity of the supporting graphite improved the conductivity by reducing the charge transfer resistance of the cathode materials. The present results concluded that the supporting graphite not only improved the electrical conductivity but also enhanced the specific capacity and the cycling performance of the pristine δ - MnO_2 . Thus, MNG is one of promising candidate cathode materials for ZIBs.

Data Availability

The authors declare that all relevant data are within the paper. Competing interests: The authors declare no potential conflict of interest.

References

- Mison, I. I. *et al.* High performance MnO_2 nanoflower electrode and the relationship between solvated ion size and specific capacitance in highly conductive electrolytes. *Mater. Res. Bull.* **57**, 221–230, <https://doi.org/10.1016/j.materresbull.2014.05.044> (2014).
- Lao-atiman, W., Julaphatachote, T., Boonmongkolras, P. & Kheawhom, S. Printed transparent thin film Zn-MnO₂ battery. *J. Electrochem. Soc.* **164**, A859–A863, <https://doi.org/10.1149/2.1511704jes> (2017).
- Suren, S. & Kheawhom, S. Development of a high energy density flexible zinc-air battery. *J. Electrochem. Soc.* **163**, A846–A850, <https://doi.org/10.1149/2.0361606jes> (2016).
- Hosseini, S. *et al.* Discharge Performance of Zinc-Air Flow Batteries Under the Effects of Sodium Dodecyl Sulfate and Pluronic F-127. *Sci. Rep.* **8**, 14909, <https://doi.org/10.1038/s41598-018-32806-3> (2018).
- Wang, J.-W., Chen, Y. & Chen, B.-Z. Synthesis and control of high-performance MnO_2 /carbon nanotubes nanocomposites for supercapacitors. *J. Alloy Compd.* **688**, 184–197, <https://doi.org/10.1016/j.jallcom.2016.07.005> (2016).
- Hosseini, S., Han, S. J., Arpornwichanop, A., Yonezawa, T. & Kheawhom, S. Ethanol as an electrolyte additive for alkaline zinc-air flow batteries. *Sci. Rep.* **8**, 11273, <https://doi.org/10.1038/s41598-018-29630-0> (2018).
- Lao-atiman, W. *et al.* Model-Based Analysis of an Integrated Zinc-Air Flow Battery/Zinc Electrolyzer System. *Frontiers in Energy Research* **7**, <https://doi.org/10.3389/fenrg.2019.00015> (2019).
- Chen, J. *et al.* Electrochemical properties of MnO_2 nanorods as anode materials for lithium ion batteries. *Electrochim. Acta* **142**, 152–156, <https://doi.org/10.1016/j.electacta.2014.07.089> (2014).
- Kim, J.-S. *et al.* High-capacity nanostructured manganese dioxide cathode for rechargeable magnesium ion batteries. *J. Power Sources* **273**, 210–215, <https://doi.org/10.1016/j.jpowsour.2014.07.162> (2015).
- Alfaruqi, M. H. *et al.* A high surface area tunnel-type α - MnO_2 nanorod cathode by a simple solvent-free synthesis for rechargeable aqueous zinc-ion batteries. *Chem. Phys. Lett.* **650**, 64–68, <https://doi.org/10.1016/j.cplett.2016.02.067> (2016).
- Kao-ian, W., Pornprasertsuk, R., Thamyongkit, P., Maiyalagan, T. & Kheawhom, S. Rechargeable Zinc-Ion Battery Based on Choline Chloride-Urea Deep Eutectic Solvent. *Journal of The Electrochemical Society* **166**, A1063–A1069, <https://doi.org/10.1149/2.0641906jes> (2019).

12. Alfuruqi, M. H. *et al.* Enhanced reversible divalent zinc storage in a structurally stable α -MnO₂ nanorod electrode. *J. Power Sources* **288**, 320–327, <https://doi.org/10.1016/j.jpowsour.2015.04.140> (2015).
13. Alfuruqi, M. H. *et al.* A layered δ -MnO₂ nanoflake cathode with high zinc-storage capacities for eco-friendly battery applications. *Electrochim. Acta* **60**, 121–125, <https://doi.org/10.1016/j.electacta.2015.08.019> (2015).
14. Lee, J., Ju, J. B., Cho, W. L., Cho, B. W. & Oh, S. H. Todorokite-type MnO₂ as a zinc-ion intercalating material. *Electrochim. Acta* **112**, 138–143, <https://doi.org/10.1016/j.electacta.2013.08.136> (2013).
15. Toupin, M., Brousse, T. & Bélanger, D. Charge storage mechanism of MnO₂ electrode used in aqueous electrochemical capacitor. *Chem. Mater.* **16**, 3184–3190, <https://doi.org/10.1021/cm049649j> (2004).
16. Feng, M. *et al.* Manganese oxide electrode with excellent electrochemical performance for sodium ion batteries by pre-intercalation of K and Na ions. *Sci. Rep.* **7**, 2219, <https://doi.org/10.1038/s41598-017-02028-0> (2017).
17. Song, J., Kim, J., Kang, T. & Kim, D. Design of a porous cathode for ultrahigh performance of a Li-ion battery: An overlooked pore distribution. *Sci. Rep.* **7**, 42521, <https://doi.org/10.1038/srep42521> (2017).
18. Wei, C., Xu, C., Li, B., Du, H. & Kang, F. Preparation and characterization of manganese dioxides with nano-sized tunnel structures for zinc ion storage. *J. Phys. Chem. Solids* **73**, 1487–1491, <https://doi.org/10.1016/j.jpcs.2011.11.038> (2012).
19. Renuka, R. & Ramamurthy, S. An investigation on layered birnessite type manganese oxides for battery applications. *J. Power Sources* **87**, 144–152 (2000).
20. Zhu, C. *et al.* One-step electrochemical approach to the synthesis of Graphene/MnO₂ nanowall hybrids. *Nano Res.* **4**, 648–657, <https://doi.org/10.1007/s12274-011-0120-2> (2011).
21. Zhou, J. *et al.* Novel synthesis of birnessite-type MnO₂ nanostructure for water treatment and electrochemical capacitor. *Ind. Eng. Chem. Res.* **52**, 9586–9593, <https://doi.org/10.1021/ie400577a> (2013).
22. Liu, J. *et al.* In situ chemical synthesis of sandwich-structured MnO₂/graphene nanoflowers and their supercapacitive behavior. *Electrochim. Acta* **173**, 148–155, <https://doi.org/10.1016/j.electacta.2015.05.040> (2015).
23. Phillips, C., Al-Ahmadi, A., Potts, S.-J., Claypole, T. & Deganello, D. The effect of graphite and carbon black ratios on conductive ink performance. *J. Mater. Sci.* **52**, 9520–9530, <https://doi.org/10.1007/s10853-017-1114-6> (2017).
24. Wongrujipairoj, K., Poolnapol, L., Arpornwichanop, A., Suren, S. & Kheawhom, S. Suppression of zinc anode corrosion for printed flexible zinc-air battery. *Phys. Status Solidi B* **254**, <https://doi.org/10.1002/pssb.201600442> (2017).
25. Chernozatonskii, L. A., Sorokin, P. B., Belova, E. É., Brüning, J. & Fedorov, A. S. Metal-semiconductor (semimetal) superlattices on a graphite sheet with vacancies. *JETP Lett.* **84**, 115–118, <https://doi.org/10.1134/s0021364006150033> (2006).
26. Li, F. *et al.* MnO₂ nanostructures with three-dimensional (3D) morphology replicated from diatoms for high-performance supercapacitors. *J. Mater. Chem. A* **3**, 7855–7861, <https://doi.org/10.1039/c5ta00634a> (2015).
27. Thapa, A. K. *et al.* Synthesis of mesoporous birnessite-MnO₂ composite as a cathode electrode for lithium battery. *Electrochim. Acta* **116**, 188–193, <https://doi.org/10.1016/j.electacta.2013.11.032> (2014).
28. Rajarao, R. & Bhat, B. R. Large scale synthesis of carbon nanofibres on sodium chloride support. *Nanomater. Nanotechnol.* **2**, 5, <https://doi.org/10.5772/50306> (2012).
29. Zhang, J., Li, Y., Wang, L., Zhang, C. & He, H. Catalytic oxidation of formaldehyde over manganese oxides with different crystal structures. *Catal. Sci. Technol.* **5**, 2305–2313, <https://doi.org/10.1039/c4cy01461h> (2015).
30. Kundu, D. *et al.* Aqueous vs. nonaqueous Zn-ion batteries: consequences of the desolvation penalty at the interface. *Energy Environ. Sci.* **11**, 881–892, <https://doi.org/10.1039/c8ee00378e> (2018).
31. Hayes, A. C., Kruus, P. & Adams, W. A. Raman spectroscopic study of aqueous (NH₄)₂SO₄ and ZnSO₄ solutions. *J. Solution Chem.* **13**, 61–75, <https://doi.org/10.1007/BF00648592> (1984).
32. Wang, J.-W., Chen, Y. & Chen, B.-Z. A synthesis method of MnO₂/activated carbon composite for electrochemical supercapacitors. *J. Electrochem. Soc.* **162**, A1654–A1661, <https://doi.org/10.1149/2.0031509jes> (2015).
33. Ji, C., Ren, H. & Yang, S. Control of manganese dioxide crystallographic structure in the redox reaction between graphene and permanganate ions and their electrochemical performance. *RSC Adv.* **5**, 21978–21987, <https://doi.org/10.1039/c5ra01455g> (2015).
34. Yang, Y.-j. *et al.* Nanostructured MnO₂/exfoliated graphite composite electrode as supercapacitors. *J. Alloy Compd.* **487**, 564–567, <https://doi.org/10.1016/j.jallcom.2009.08.008> (2009).
35. Li, J. *et al.* Improved Li-ion diffusion process in TiO₂/rGO anode for lithium-ion battery. *J. Alloy Compd.* **727**, 998–1005, <https://doi.org/10.1016/j.jallcom.2017.08.121> (2017).
36. Simon, P., Gogotsi, Y. & Dunn, B. Where do batteries end and supercapacitors begin. *Science* **343**, 1210–1211 (2014).
37. Chen, D. *et al.* Probing the charge storage mechanism of a pseudocapacitive MnO₂ electrode using in operando raman spectroscopy. *Chem. Mater.* **27**, 6608–6619, <https://doi.org/10.1021/acs.chemmater.5b03118> (2015).
38. Guo, X. *et al.* A hollow-structured manganese oxide cathode for stable Zn-MnO₂ batteries. *Nanomaterials* **8**, <https://doi.org/10.3390/nano8050301> (2018).
39. Alfuruqi, M. H. *et al.* Structural transformation and electrochemical study of layered MnO₂ in rechargeable aqueous zinc-ion battery. *Electrochim. Acta* **276**, 1–11, <https://doi.org/10.1016/j.electacta.2018.04.139> (2018).
40. Qiu, W. *et al.* High-performance flexible quasi-solid-state Zn-MnO₂ battery based on MnO₂ nanorod arrays coated 3D porous nitrogen-doped carbon cloth. *J. Mater. Chem. A* **5**, 14838–14846, <https://doi.org/10.1039/c7ta03274a> (2017).
41. Alfuruqi, M. H. *et al.* Electrochemically induced structural transformation in a γ -MnO₂ cathode of a high capacity zinc-ion battery system. *Chem. Mater.* **27**, 3609–3620, <https://doi.org/10.1021/cm504717p> (2015).
42. Islam, S. *et al.* Carbon-coated manganese dioxide nanoparticles and their enhanced electrochemical properties for zinc-ion battery applications. *J. Energy Chem.* **26**, 815–819, <https://doi.org/10.1016/j.jechem.2017.04.002> (2017).
43. Xu, C., Li, B., Du, H. & Kang, F. Energetic zinc ion chemistry: the rechargeable zinc ion battery. *Angew. Chem. Int. Ed. Engl.* **51**, 933–935, <https://doi.org/10.1002/anie.201106307> (2012).
44. Liu, H. *et al.* Kinetic study on LiFePO₄/C nanocomposites synthesized by solid state technique. *J. Power Sources* **159**, 717–720, <https://doi.org/10.1016/j.jpowsour.2005.10.098> (2006).
45. Bard, A. J. & Faulkner, L. R. *Electrochemical Methods*. 2 edn, 211 (JOHN WILEY & SONS, INC. 2001).
46. Li, H. *et al.* Dual-carbon confined SnO₂ as ultralong-life anode for Li-ion batteries. *Ceram. Int.* **45**, 7830–7838, <https://doi.org/10.1016/j.ceramint.2019.01.090> (2019).
47. Cao, Q. *et al.* A novel carbon-coated LiCoO₂ as cathode material for lithium ion battery. *Electrochim. Acta* **9**, 1228–1232, <https://doi.org/10.1016/j.electacta.2007.01.017> (2007).

Acknowledgements

SKS acknowledged the scholarship from “The 100th Anniversary Chulalongkorn University Fund for Doctoral Scholarship” as well as “The 90th Anniversary Chulalongkorn University, Ratchadapisek Sompote Fund”. Also, SKH acknowledged Thailand Research Fund (RSA6180008) and Ratchadapisek Sompote Fund, Chulalongkorn University.

Author Contributions

SKH conceived the experiments, SKS conducted the experiments. Data analyses were done by SKS with consultation with SKH. The paper was written by SKS and SKH, and all authors contributed to the subsequent drafts and revision. All authors reviewed the manuscript.

Additional Information

Supplementary information accompanies this paper at <https://doi.org/10.1038/s41598-019-44915-8>.

Competing Interests: The authors declare no competing interests.

Publisher's note: Springer Nature remains neutral with regard to jurisdictional claims in published maps and institutional affiliations.



Open Access This article is licensed under a Creative Commons Attribution 4.0 International License, which permits use, sharing, adaptation, distribution and reproduction in any medium or format, as long as you give appropriate credit to the original author(s) and the source, provide a link to the Creative Commons license, and indicate if changes were made. The images or other third party material in this article are included in the article's Creative Commons license, unless indicated otherwise in a credit line to the material. If material is not included in the article's Creative Commons license and your intended use is not permitted by statutory regulation or exceeds the permitted use, you will need to obtain permission directly from the copyright holder. To view a copy of this license, visit <http://creativecommons.org/licenses/by/4.0/>.

© The Author(s) 2019